

International Journal of Computational Intelligence and Applications
© World Scientific Publishing Company

INTERACTIVE REGISTRATION OF INTRACELLULAR VOLUMES WITH RADIAL BASIS FUNCTIONS

SHIN YOSHIZAWA SATOKO TAKEMOTO

*Bio-Research Infrastructure Construction Team, VCAD System Research Program, RIKEN,
2-1, Hirosawa, Wako, Saitama, 351-0198, Japan*

MIWA TAKAHASHI

*Department of Biochemistry, University of Geneva,
30 quai Ernest-Ansermet, CH-1211, Geneva, Switzerland*

MAKOTO MUROI SAYAKA KAZAMI

*Antibiotics Laboratory, Advanced Science Institute, RIKEN,
2-1, Hirosawa, Wako, Saitama, 351-0198, Japan*

HIROMI MIYOSHI

*Computational Cell Biomechanics Team, VCAD System Research Program, RIKEN,
2-1, Hirosawa, Wako, Saitama, 351-0198, Japan*

HIDEO YOKOTA

*Bio-Research Infrastructure Construction Team, VCAD System Research Program, RIKEN,
2-1, Hirosawa, Wako, Saitama, 351-0198, Japan*

We propose a novel approach to 3D image registration of intracellular volumes. The approach extends a standard image registration framework to the curved cell geometry. An intracellular volume is mapped onto another intracellular domain by using two pairs of point set surfaces approximating their nuclear and plasma membranes. The mapping function consists of the affine transformation, tetrahedral barycentric interpolation, and least-squares formulation of radial basis functions for extracted cell geometry features. An interactive volume registration system is also developed based on our approach. We demonstrate that our approach is capable to create cell models containing multiple organelles from observed data of living cells.

Keywords: Intracellular Volume; Live Cell Imaging; Non-rigid Registration; Least-squares RBF.

1. Introduction

Recent advances in live cell imaging make it possible to observe the organelles^a in living cells as 3D images. Quantitative analysis of such *intracellular volumes* has thus become important in cell biology [10]. Also numerical simulations based on the intracellular volumes are becoming popular in recent biophysics and systems biology. Therefore, constructing

^aIn this paper, we use a word of *organelle* for objects in living cells such as organelles, cytoskeletons, vesicles, etc. for the sake of simplicity.

2 S. YOSHIZAWA, S. TAKEMOTO, M. TAKAHASHI, M. MUROI, S. KAZAMI, H. MIYOSHI, and H. YOKOTA

the cell shape models which include multiple organellar structures has considerable attentions in order to simulate intracellular events realistically. Intracellular volumes are usually determined under a confocal laser microscope with fluorescent organellar markers. Unfortunately, simultaneous observation of many different fluorescent markers is not possible because of technical difficulties with microscopes, fluorescent markers, and cell conditions ([4, 14], and references therein). Only one or two fluorescent markers are usually employed in cell biology experiments to avoid the problems caused by increasing markers.

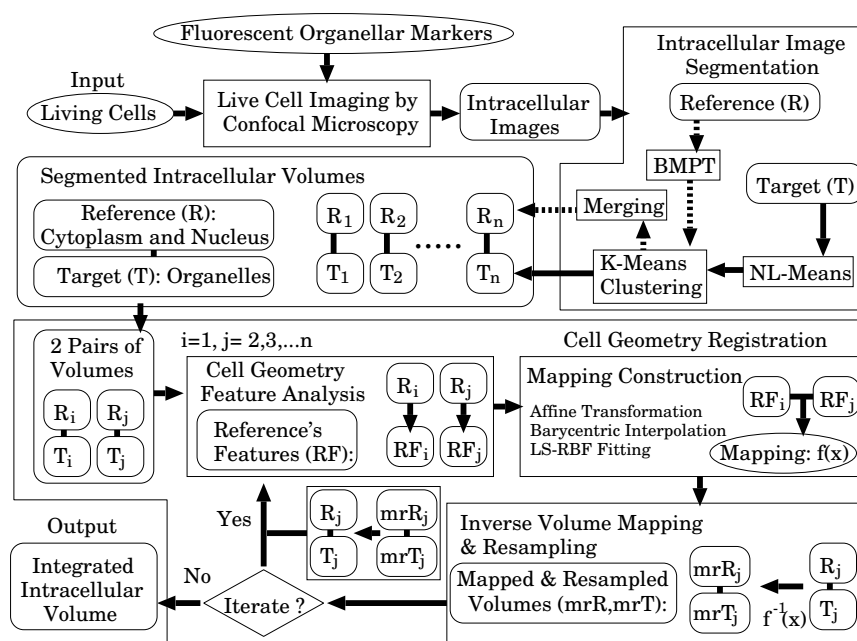


Fig. 1. Intracellular volume registration flowchart.

Our approach. In this paper^b, we propose a novel approach to *intracellular volume registration* (the non-rigid alignment of separately observed 3D images of the different intracellular objects) as an alternative solution to overcoming the difficulties of simultaneous observation. The main idea behind the approach is to construct a function that maps one intracellular domain to another by using the geometric feature points extracted from the cell's nuclear and plasma membranes. Figure 1 illustrates a flowchart of our approach. First, we observe the cytoplasm together with its nucleus as a reference volume, and simultaneously the objective organelle as its corresponding target volume. The cytoplasm and nucleus are chosen because their topological configuration during interphase, that of a sphere envelop-

^bIt is an extension of our previous work [42]. The main difference from [42] includes the improvements in our least-squares RBF formulation with self-intersection fairing in addition to more detailed description of the proposed approach.

ing another sphere, is simple. Then these regions are isolated from their backgrounds to produce segmented reference volumes. Next, the nuclear and plasma membranes are approximated by a pair of point set surfaces sampled on the boundaries of the isolated regions, and their geometric features are extracted. Next, a mapping function between a pair of reference volumes is constructed by applying affine transformation, tetrahedral barycentric interpolation, and least-squares radial basis function (RBF) fitting methods to the extracted features. Finally, the constructed mapping function is applied to one of the reference and its corresponding target volumes.

Contribution and benefit. The goal of this study was to generate a numerical cell model including multiple organelles that represents living cell as close as possible. Such a model is useful for presenting combined organellar information to biologists and for running numerical cell simulations. Our approach is capable of integrating individually observed intracellular objects, as demonstrated in Section 5. The study presents a new approach to overcoming the difficulties of simultaneous observation of many different fluorescent markers. Its technical contribution includes an interactive intracellular volume registration system, adapting the least-squares RBF to cell geometry, and a novel method for extracting cell geometry features; this method semi-automatically provides feature point correspondences.

Paper organization. The rest of paper is organized as follows. Section 2 briefly describes previous work on image registration. We present how to segment reference and target volumes in Section 3. Section 4 describes the cell geometry registration technique. Our numerical experiments are explained in Section 5. We conclude the paper in Section 6.

2. Previous Work on Image Registration

Image registration is popular and well-studied in computer vision and image processing communities [12, 18, 22]; see [44, 45], and references therein for general image registration techniques. The high-dimensional extensions of such techniques are often used in bio-medical image processing [23, 34, 35] to merge CT, MRI, and microscopic images. Non-rigid transformations are necessary for such bio-medical data because of the complex curved geometry of the objects of study. In particular, traditional RBF fitting methods have been used for non-rigid registration [11, 33, 36] and many other tasks. On the other hand, non-rigid transformations for intracellular volumes had not been studied until very recently [20, 24, 41] because the objects in living cells are usually not solid; they are also both topologically and geometrically complex and vary with time. Therefore, intracellular volume registration is a difficult problem, but it is a promising research subject because of rapid advances in live-cell-imaging technology.

Mattes et al. employed a thin-plate spline transformation model with landmarks for their 2D intracellular image registration [24]. Kim et al. proposed a non-rigid registration approach to intracellular volumes of different cell nuclei [20]; the approach was based on the so-called demons algorithm [38]. Yang et al. extended this approach to segmented volumes [41]. However they considered only cell nuclei, which, unlike nuclear and plasma

4 *S. YOSHIZAWA, S. TAKEMOTO, M. TAKAHASHI, M. MUROI, S. KAZAMI, H. MIYOSHI, and H. YOKOTA*

membranes, have a simple topological and geometrical configuration. Our approach is capable of transforming a volume domain (including organelles) between the nuclear and plasma membranes, whereas the previous approaches [20, 24, 41] consider only the volume domain inside the nucleus (with no organelles).

In contrast with the previous RBF techniques [11, 33, 36] used in CT and MRI image registration, our approach employs a least-squares RBF fitting method that is popular in geometry processing such as surface reconstruction [30] and shape editing [5].

3. Intracellular Image Segmentation

To construct a function mapping one volume onto another, we first isolate the nuclear and cytoplasmic regions from their backgrounds. The target organellar region within the cytoplasm is segmented for further quantitative analysis, although the segmented target volume is not necessary to construct the mapping function.

The intracellular volumes generated from observations of living cells contain noise. Their low signal-to-noise ratio has causes, including poor microscope resolution, Brownian motion, blurring, movement of organelles, and bleaching of fluorescent markers [4]. Moreover, small variations made to the observation settings for different organelles introduce inconsistencies in the same feature among images. Such noise and inconsistency make it difficult to achieve high-quality segmentation of intracellular volumes. Our segmentation technique incorporates noise reduction methods and clustering the filtered image.

Image details are important in isolating organelles for quantitative analysis. On the other hand, image smoothness and robustness to small perturbations are required for segmenting the nucleus and cytoplasm in order to construct a good mapping function. Therefore, we use two image denoising filters for the targets (organelles) and their corresponding references (cytoplasm and nucleus): Non-Local Means (NL-Means) [6] for targets and the Block-Median Pyramidal Transform (BMPT) [28] for the references. BMPT filter is an extension of the pyramidal median transform [21] which was developed in astronomical image analysis in order to isolating global regions of various illuminating points [37]. Since the nuclear and cytoplasmic regions also consist of such illuminating points representing sets of fluorescent proteins, the BMPT filter was chosen to produce nicely smoothed volumes. The multiresolution strategy of BMPT provides robustness for constructing our mapping function. NL-Means filter preserves detail while reducing noise, and often used in image segmentation [1, 13, 19]. Figure 2 shows advantages of the use of two different filtering schemes in our segmentation technique.

After the filters are applied, the organellar, cytoplasmic, nuclear, and background regions are segmented by unsupervised K-means clustering [27] for the filtered image intensities. Finally, the unwanted isolated regions are labeled and merged to reproduce the topological configuration of cytoplasm and nucleus. Figure 3 illustrates the isolation of the nucleus and cytoplasm from their backgrounds.

Image segmentation has been one of the most intensive fields of study in image processing and computer vision [1, 17, 25, 43]. The conventional segmentation methods of intracellular images [8, 9, 16, 26] have been mainly designed to identify the entire cytoplas-

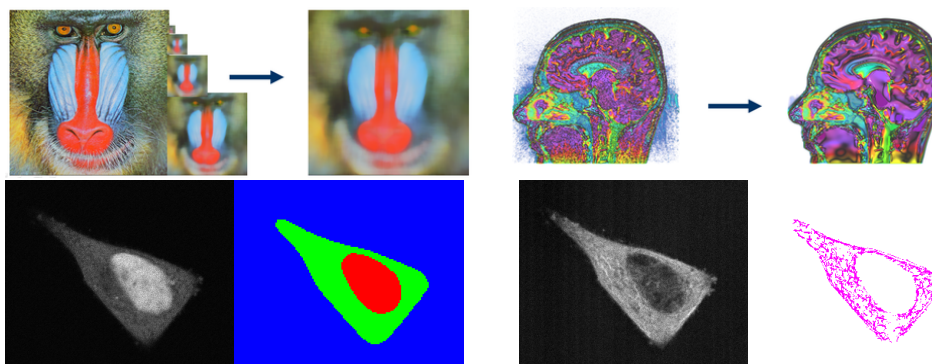


Fig. 2. Noise robust and detail-preserving segmentations. Left: BMPT filtering of a 2D image (top) and segmentation of a reference volume (bottom, microtubule's cytoplasm and nucleus). Right: NL-Means filtering of a MRI volume (top) and segmentation of a target volume (bottom, microtubules).

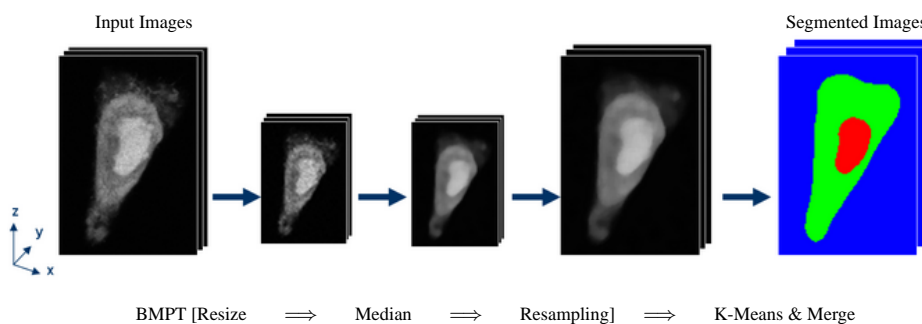


Fig. 3. Segmentation of cytoplasm and nucleus.

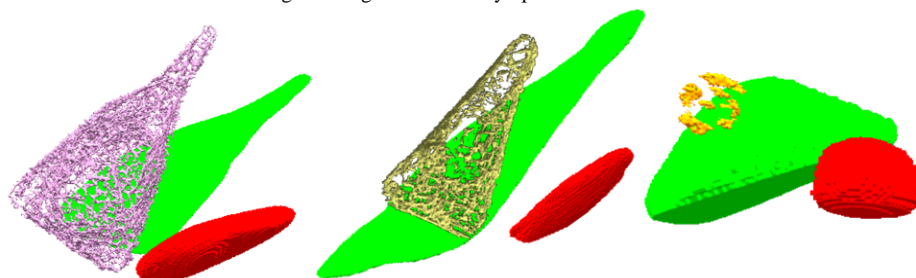


Fig. 4. Segmented intracellular volumes by our technique: microtubules (left), actin filaments (center), and Golgi apparatus (right). In this research, we assessed the quality of segmentation by visual inspection of cell biologists.

mic or nuclear regions. Unfortunately, applying these methods to our reference volumes is not straightforward. For example, a great amount of training data set for machine learning [16], the user specified initial segmentation [26], extending the method of [8] to 3D, and some optimization method to place the source and sink positions of graph cut algorithm [9] are required in order to use these methods in our purpose. On the other hand, our simple multiresolution strategy provides us satisfactory results as demonstrated in Figures 3 and 4. In addition, our technique is applicable to a more wide range of organelle volumes.

4. Cell Geometry Registration

Our registration technique is based on extending a standard image registration framework summarized by Zitová et al. [45] to the curved cell geometry (Fig. 5). Our technique works as follows. First, the geometric features of each reference volume are extracted automatically. Next, a mapping function $f : (u, v, w) \rightarrow (x, y, z)$ between two different intracellular domains $(u, v, w) \in \Omega_1$ and $(x, y, z) \in \Omega_2$ is constructed by using the extracted features of a pair of reference volumes. In this mapping construction phase, the affine transformation and tetrahedral barycentric interpolation are employed to align the reference volumes roughly, and then the least-squares RBF provides the final detailed mapping. The choice of the mapping methods and adjustments of the extracted features are interactively performed by a user in our technique. Next, one of the target organellar volumes is mapped onto another target domain via the constructed mapping function with resampling. We use the inverse mapping with resampling (nearest neighbor and tri-cubic interpolation) which is a common method to obtain transformed images in image processing [15, Sect. 2.6.5]. Finally, the resampled volume is integrated to another volume. The following subsections describe the methods in our technique.

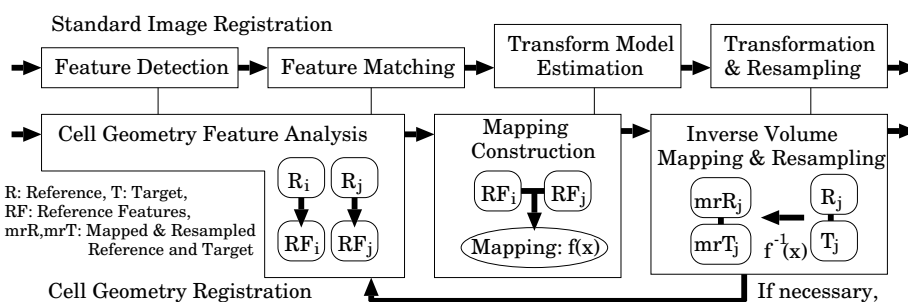


Fig. 5. Our technique inherits the framework of [45] consisting of four steps: feature detection, feature matching, transform model estimation, and transformation and resampling.

4.1. Cell Geometry Feature Analysis

Consider a given pair of plasma membranes represented by the point set surfaces ∂_1 and ∂_2 , which live in domains Ω_1 and Ω_2 , respectively. Let c_1 and c_2 be the centers of gravity of ∂_1 and ∂_2 . Principal Component Analysis (PCA) of ∂_1 and ∂_2 gives us the pair of corresponding principal axes $\{t_1^1, t_2^1, t_3^1\}$ and $\{t_1^2, t_2^2, t_3^2\}$. The same computations are applied to the corresponding nuclear membranes. Then the following feature and sub-feature points are extracted for the two pairs of nuclear and plasma membranes (four point set surfaces).

Let ∂ , c , and $\{t_1, t_2, t_3\}$ be one of the point set surfaces, its center of gravity, and its principal axes, respectively. Assume that t_1 is the longest PCA direction of ∂ , and t_3 is perpendicular to the cell face on the cover-glass (xy -plane). If the calculated t_3 is far from being a normal vector of the xy -plane, we compute t_1 and t_2 by averaging 2D PCA axes of ∂ 's contour curves instead of the 3D PCA axes. The contour curves on ∂ are obtained by extracting sectional curves along the z -axis. Then, t_3 is obtained by a cross product of t_1 and t_2 .

We consider three feature point sets sampled on ∂ as shown in the images (a), (b), and (c) of Figure 6. The three sets, in which consist of the six, twenty six, and eleven feature points, are located on each of nuclear and plasma membranes. The feature points are obtained by calculating intersections of ∂ with the rays (half-lines) from \mathbf{c} . The first two sets (a,b) are easily calculated from the PCA directions (six rays) and their bisectors of adjacent PCA directions (twenty six rays). The last set (c) is specialized to a triangle-patterned cell shape. We employed a triangle micro-patterned substrate in our live-cell-imaging experiments, because it reduces complexity of the cell's plasma membrane shape. Their corresponding eleven rays in (c) are parallel to $\pm\mathbf{t}_{2,3}$, $\chi(\mathbf{t}_1)$, $\pm\mathbf{t}_{2,3} + \chi(\mathbf{t}_1)$, and $\chi(\pm\mathbf{t}_2 - \mathbf{t}_1)$, where $\chi(\mathbf{t}) = (\operatorname{argmax}_{\mathbf{x} \in \partial} \langle \mathbf{x} - \mathbf{c}, \mathbf{t} \rangle) - \mathbf{c}$. Here the vector function $\chi(\mathbf{t})$ gives us the farthest direction with respect to a given vector \mathbf{t} , and the multiple sub-index $\mathbf{t}_{i,j}$ corresponds to \mathbf{t}_i and \mathbf{t}_j . The sub-feature points are sampled on the geodesics between the feature points on ∂ .

Note that the correspondences between two sets of feature points on ∂_1 and ∂_2 are automatically obtained by specifying the correspondence of the PCA directions $\{\mathbf{t}_1^1, \mathbf{t}_2^1, \mathbf{t}_3^1\}$ and $\{\mathbf{t}_1^2, \mathbf{t}_2^2, \mathbf{t}_3^2\}$, because the feature points (also sub-feature points) are automatically generated after the PCA directions are obtained. This semi-automatic correspondence generation reduces a lot of manual registration, and it gives us an intuitive and interactive user interface, as shown in Figures 6 (a,b,c) and 12. Moreover, these feature points are useful to generate the RBF centers used in our RBF fitting method as shown in Figure 6 (d).

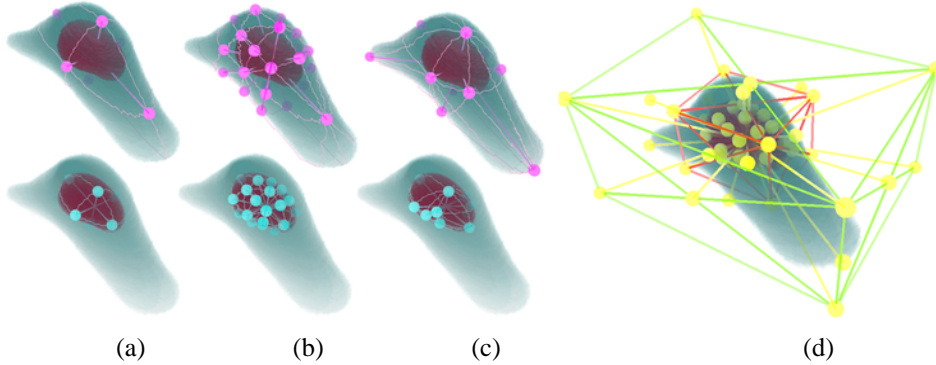


Fig. 6. (a,b,c): extracted feature and sub-feature points based on PCA of nuclear (bottom) and plasma (top) membranes. (d): automatic RBF center generation by using the extracted features with two bounding boxes of the cytoplasm and nucleus.

4.2. Affine Transformation with PCA

When the shapes of two pairs of nuclear and plasma membranes are similar to each other, the global mapping models [45] are the simplest way to obtain proper registration results. Once the PCA directions are obtained, constructing one of the most frequently used global mapping model to the curved cell geometry is as follows. The affine transformation $f(\mathbf{x})$, which transforms a point $\mathbf{x} \in \Omega_1$ to the domain Ω_2 , is automatically constructed via PCAs of ∂_1 and ∂_2 :

$$f(\mathbf{x}) = \mathbf{A}(\mathbf{x} - \mathbf{c}_1) + \mathbf{c}_2, \quad \mathbf{A} = (\mathbf{t}_1^2, \mathbf{t}_2^2, \mathbf{t}_3^2)(\mathbf{t}_1^1, \mathbf{t}_2^1, \mathbf{t}_3^1)^{-1}.$$

8 S. YOSHIZAWA, S. TAKEMOTO, M. TAKAHASHI, M. MUROI, S. KAZAMI, H. MIYOSHI, and H. YOKOTA

In addition, our technique allows a user to manually specify a corresponding pair of four points on the plasma membrane surfaces (Fig. 7) for the affine transformation.

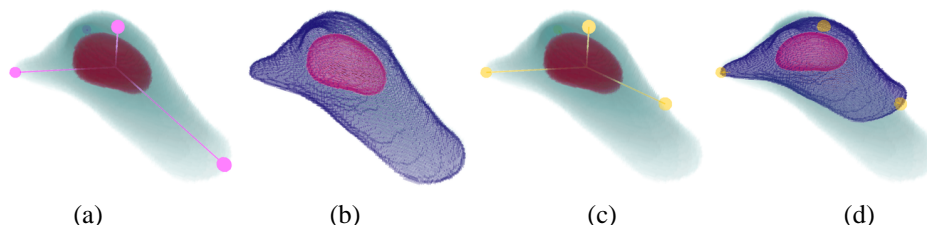


Fig. 7. A manual registration example via affine transformation with a pair of four points. (a,c): the pair of four points on the plasma membrane surfaces. (b): the point set surfaces approximating the nuclear and plasma membranes. (d): the affine transformed point set surfaces via the pair of four points shown in (a) and (c).

4.3. Tetrahedral Barycentric Interpolation

Barycentric interpolation and its extensions are useful to form a mapping between two polyhedra, because they have many properties desirable for a feature-preserving interpolation [3]. In our case, valid tetrahedrization can be applied to the bounding boxes of the cytoplasm and nucleus without any degeneration of a tetrahedron because of its topological configuration such as a sphere enveloping another sphere (Fig. 8).

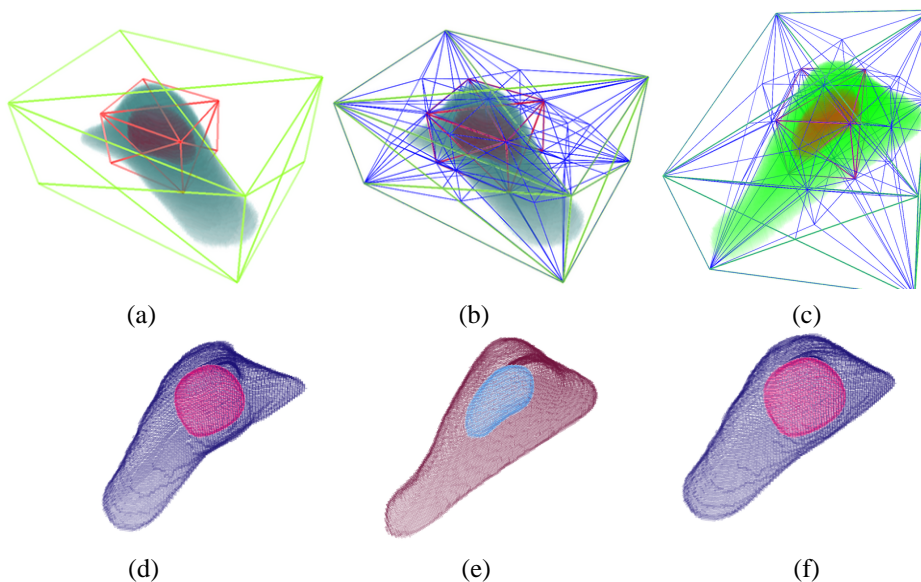


Fig. 8. Tetrahedrizations and their barycentric interpolation. (a): the cytoplasmic and nuclear bounding boxes and its corresponding tetrahedrization (b). (d,e): the point set surfaces of (b) and another volume (c), respectively. (f): the interpolated point set surfaces via the tetrahedrizations of (b) and (c) with their barycentric coordinates.

Six hexahedra are generated by connecting the corresponding corners of the nuclear and cytoplasmic bounding boxes. The tetrahedrization consists of seven hexahedra (the generated six plus the nucleus bounding box), each of which consists of twenty four tetrahedra.

The tetrahedra in each hexahedron are generated by adding a point to the hexahedron center and six points to its face centers, and then connecting these points with the hexahedron vertices.

The mapping function between a pair of tetrahedrizations in Ω_1 and Ω_2 is constructed by a set of tetrahedral barycentric interpolations. The location of a point inside of the tetrahedron is given by the volume ratio of four tetrahedra as a generalization of 2D triangle barycentric coordinates.

4.4. Least-Squares RBF Fitting

The following RBF fitting scheme is employed in our technique in order to handle locally deformed volumes which are difficult to obtain appropriate registration results by the affine transformation and tetrahedral barycentric interpolation methods.

For a given pair of point sets $\{\mathbf{x}_i\}_{i=1}^n \in \Omega_1$ and $\{\mathbf{y}_i\}_{i=1}^n \in \Omega_2$ which represents a pair of the reference volumes, we would like to find a vector-valued function $\mathbf{y} = f(\mathbf{x})$ such that $f(\mathbf{x}_k) = \mathbf{y}_k$. The solution by a standard RBF is given by

$$\hat{f}(\mathbf{x}) = g(\mathbf{x}) + \sum_{j=1}^n \hat{\lambda}_j \varphi(|\mathbf{x} - \mathbf{x}_j|), \quad \hat{\lambda}_j \in \mathbb{R}^3, \quad (1)$$

where $\hat{\lambda} = \{\hat{\lambda}_i\}_{i=1}^n$ are the RBF coefficients and $g(\mathbf{x})$ is a low degree trivariate polynomial depending on the choice of $\varphi(\cdot)$. For example, $\varphi(\cdot) = |\cdot|$ and $\varphi(\cdot) = |\cdot|^3$ with the linear and quadratic polynomials in (1) correspond to the biharmonic and triharmonic RBFs, respectively. The interpolation $\hat{f}(\mathbf{x}) = \mathbf{y}$ and orthogonality $\sum_{j=1}^n \hat{\lambda}_j \mathbf{x}_j = \sum_{j=1}^n \hat{\lambda}_j = \mathbf{0}$ conditions lead a linear system

$$\begin{pmatrix} \Phi & \mathbf{Q} \\ \mathbf{Q}^T & \mathbf{0} \end{pmatrix} \begin{pmatrix} \hat{\lambda} \\ \mathbf{g} \end{pmatrix} = \begin{pmatrix} \mathbf{y} \\ \mathbf{0} \end{pmatrix}, \quad \Phi_{ij} = \varphi(|\mathbf{x}_i - \mathbf{x}_j|), \quad \mathbf{Q}_{ij} = Q_j(\mathbf{x}_i),$$

where $\mathbf{g} = \{g_k\}_{k=1}^l$ are the coefficients of $g(\mathbf{x})$ and $Q_k(\mathbf{x}_i)$ is a basis of $g(\mathbf{x}_i)$ which corresponds to g_k .

To fit the RBF robustly, we use the following least-squares RBF formulation. Consider the so-called RBF centers $\xi = \{\xi_j\}_{j=1}^m$, which consist of one of the feature point sets in Ω_1 and the bounding box vertices of the cytoplasm and nucleus (Fig. 6, (d)). Let $\mathbf{p} = \{\mathbf{p}_i\}_{i=1}^n$ be a set of feature and sub-feature points of the cytoplasm and nucleus in Ω_1 (two point set surfaces) and let $\mathbf{q} = \{\mathbf{q}_i\}_{i=1}^n$ be the corresponding set of feature and sub-feature points in Ω_2 . Then, the LS-RBF is given by

$$f(\mathbf{x}) = g(\mathbf{x}) + \sum_{j=1}^m \lambda_j \varphi(|\mathbf{x} - \xi_j|), \quad \lambda_j \in \mathbb{R}^3, \quad n \gg m,$$

where we use $\varphi(u) = u^3$ and a linear polynomial for $g(\mathbf{x})$. The polynomial and RBF coefficients $\lambda = \{\lambda_j\}_{j=1}^m$ and $\mathbf{g} = (g_1, g_2, g_3, g_4)$ are obtained by solving a least-squares system of linear equations

$$(\lambda, \mathbf{g})^T = (\mathbf{A}^T \mathbf{A})^{-1} \mathbf{A}^T (\mathbf{q}, \mathbf{0})^T. \quad (2)$$

10 S. YOSHIZAWA, S. TAKEMOTO, M. TAKAHASHI, M. MUROI, S. KAZAMI, H. MIYOSHI, and H. YOKOTA

Here the rectangular matrix \mathbf{A} is composed by satisfying the following interpolation and orthogonality conditions: $f(\mathbf{p}) = \mathbf{q}$ and $\sum_{j=1}^m \lambda_j \xi_j = \sum_{j=1}^m \lambda_j = \mathbf{0}$. Thus we have

$$\mathbf{A} = \begin{pmatrix} \Phi_{11} & \Phi_{12} & \cdots & \Phi_{1m} & 1 & p_1^x & p_1^y & p_1^z \\ \Phi_{21} & \Phi_{22} & \cdots & \Phi_{2m} & 1 & p_2^x & p_2^y & p_2^z \\ \vdots & \vdots & \ddots & \vdots & \vdots & \vdots & \vdots & \vdots \\ \Phi_{n1} & \Phi_{n2} & \cdots & \Phi_{nm} & 1 & p_n^x & p_n^y & p_n^z \\ 1 & 1 & \cdots & 1 & 0 & 0 & 0 & 0 \\ \xi_1^x & \xi_2^x & \cdots & \xi_m^x & 0 & 0 & 0 & 0 \\ \xi_1^y & \xi_2^y & \cdots & \xi_m^y & 0 & 0 & 0 & 0 \\ \xi_1^z & \xi_2^z & \cdots & \xi_m^z & 0 & 0 & 0 & 0 \end{pmatrix}, \quad \begin{aligned} \Phi_{ij} &= \varphi(|\mathbf{p}_i - \xi_j|), \\ \xi_i &= (\xi_i^x, \xi_i^y, \xi_i^z), \\ \mathbf{p}_i &= (p_i^x, p_i^y, p_i^z). \end{aligned}$$

The resulting RBF is the so-called pseudo-cubic function [39]. Since the RBF may generate space folding (Fig. 9), the linear regression RBF scheme [7, 31] is used as

$$(\mathbf{A}^T \mathbf{A}) \Rightarrow (\alpha \beta \begin{pmatrix} \mathbf{I} & \mathbf{0} \\ \mathbf{0} & \mathbf{0} \end{pmatrix}) + (\mathbf{A}^T \mathbf{A})$$

to reduce self-intersections, where \mathbf{I} is a $m \times m$ identity matrix, β is an absolute maximum value of a diagonal element subset $\{(\mathbf{A}^T \mathbf{A})_{ii}\}_{i=1}^m$, and α is a user-specified smoothness parameter. Figure 10 demonstrates the self-intersection fairing results with varying α .

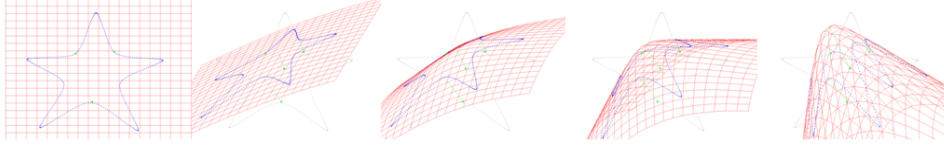


Fig. 9. 2D examples of foldover via the RBF. We can see space folding from the left to right images.

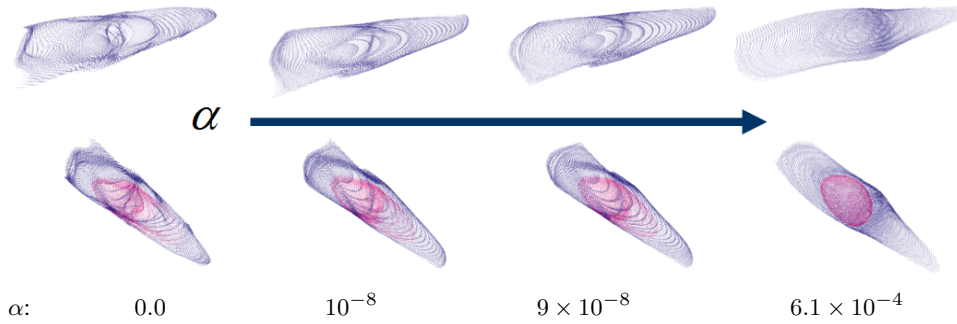


Fig. 10. Self-intersection fairing by the linear regression. Increasing α (left to right) interactively penalizes self-intersections caused by LS-RBF. Top and bottom images correspond to top and bottom views of the mapped point set surfaces.

The equation (2) is numerically solved by using the LU decomposition [32]. Note that we only need to decompose the $(m+4) \times (m+4)$ square matrix $(\mathbf{A}^T \mathbf{A})$ when ξ and \mathbf{p} are changed by user interactions. The xyz -components of (λ, \mathbf{g}) are obtained by separately

applying backward substitution of each component of $\mathbf{A}^T(\mathbf{q}, \mathbf{0})^T$ with the decomposed matrix. The point numbers of \mathbf{p} , \mathbf{q} , ξ , ∂_1 , and ∂_2 are relatively smaller than the voxel numbers of reference volumes, therefore we update and visualize the point set surfaces during the user interactions instead of constructing the mapped volume. Since the backward substitution is quite fast, constructing and applying our LS-RBF to the point set surfaces are sufficiently fast for interactive registration. Figure 11 shows the volumes and their corresponding point set surfaces mapped via our LS-RBF.

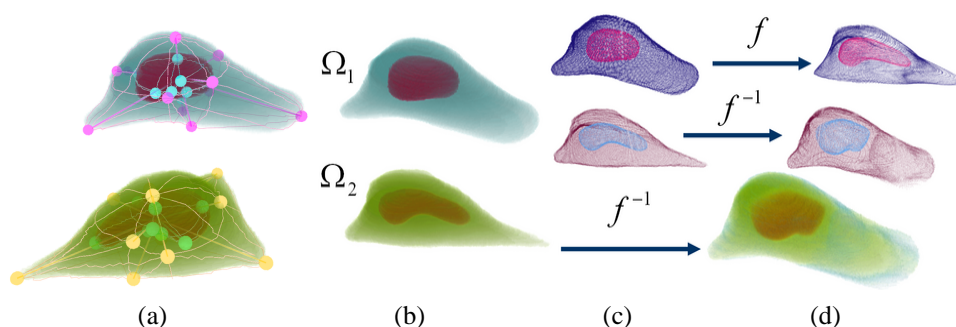


Fig. 11. LS-RBF fitting with inverse mapping. (a): two pairs of feature and sub-feature points on the nuclear and plasma membranes. (b): two pairs of cytoplasm with nucleus. (c): boundary point sets approximating the plasma and nuclear membranes. (d): point sets and volume transformed via the LS-RBF f and its inverse mapping f^{-1} .

4.5. Interactive Registration System

We have developed a computer-aided registration system based on our registration technique. The system is implemented by using Java Development Kit with Java3D. Figure 12 illustrates a graphical user interface (GUI) of the system.

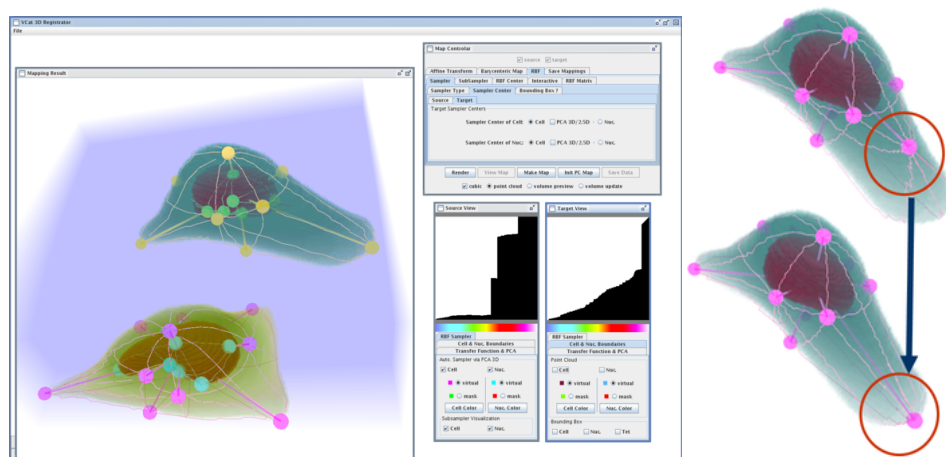


Fig. 12. Interactive registration system GUI.

The system includes a 3D volume rendering window in order to visualize input reference volumes. This 3D rendering window provides the interactive GUI to repositioning

the feature points restricted on the nuclear and plasma membrane surfaces of the cell (Fig. 12, right). Changes of visualization and registration settings by a user are immediately reflected on the 3D rendering window. Then, the system performs the cell geometry feature extraction method and the mapping methods described above. Finally, the system updates the 3D rendering window according to the results of the methods. This interactive system provides intuitive registration of intracellular volumes.

5. Results

In experiments, we used HeLa cells cultured on a triangular micro-patterned substrate produced by the photochemical method [29] to regularize the observed living HeLa cell shapes. A fluorescent-protein-tagged nuclear localization signal (NLS) plasmid was employed to characterize the cytoplasm and nucleus. The parameters of the BMPT and NL-Means for different organelles were decided on by cell biologists, who selected the result that they considered to be the best approximation of the organelles by using varying parameters to filter the results. All numerical experiments were performed on a Core2Duo PC (2.4 GHz, no parallelization is used) with 8 GB RAM.

Figures 13, 14, and 15 show our registration results, in which the resulting volumes consist of $304 \times 508 \times 116$ voxels. The shapes and positions of the mapped organellar volumes are reasonable, even though the geometric configurations of the cytoplasm and nucleus are complex. We examined our registration approach to twenty seven pairs of the intracellular volumes. The segmentation and registration qualities were visually inspected by seventeen cell biologists in terms of intracellular morphology.

The resulting volumes provide us the combined geometry and positions of organelles among the individually observed cells. For example, we can easily see the relative positions of cytoplasm, nucleus, and Golgi apparatus among varying time in the bottom images of Figure 15, whereas these relationships are not clear in the top images because of different nuclear and plasma membrane shapes. Also 3D combined information of complex intracellular objects as actin filaments and microtubules shown in Figure 14 is difficult to imagine without registration of them. This is an advantage over raw image data and the previous intracellular image registration approaches [20, 24, 34, 41] for analyzing organellar dynamics and functions.

Unlike the landmarks used in [24] and the image intensity of cell nuclei employed in [20, 41], our approach does not depend on the target organellar volumes explicitly. Therefore, our registration results are much robust with respect to topology changes of observation targets which biologist would like to analyze. Note that the techniques of [20, 41] are not able to merge the organelles. Compared with recent image registration techniques [33, 35, 36], our approach is preferable for mapping intracellular volumes because of our method for extracting cell geometry features.

Our use of the point set surfaces gives us the interactive registration rate (about 1-10 microseconds) for the computations that require user manipulation, such as adjustments to the corresponding points in the LS-RBF fitting, the corresponding mapping calculations, and visualization of the mapped point set surfaces. The inverse volume resampling requires

a few minutes. One intracellular volume registration task can be completed within 5-20 minutes by an experienced user with our system.

Discussion. In this research, accuracy and quality of the registration results depend on visual inspections of individual cell biologists who acquired the corresponding intracellular volumes. Unfortunately their criteria are heuristic, because a ground truth of organellar shapes is not mathematically formalized in current cell biology. Thus, we used their educated guesses for validating the registration results. In future work, combining the machine learning techniques [2, 40] with our approach is promising in order to incorporate such perceptual knowledge on organellar shapes more systematically.

Future work includes the intracellular registration during cell division. Also implementing physically-based transformations such as visco-hyperelastic deformations to our registration approach is interesting, although it is difficult to estimate physical parameters in living cells.

6. Conclusion

In this paper, we proposed a novel approach to intracellular volume registration based on constructing a function mapping one intracellular volume onto another by analyzing the geometry of the plasma and nuclear membranes. This approach allows us to integrate the volumes of individually observed organelles, which is difficult in conventional live cell imaging. We presented three mapping methods (affine transformation, tetrahedral barycentric interpolation, and least-squares radial basis function fitting) specialized to intracellular volumes. The interactive intracellular volume registration system was also developed. Besides its benefits to quantitative analysis in cell biology, our approach is useful for cell simulations based on real-world data.

Acknowledgements

We would like to thank Yutaka Ohtake for a valuable discussion and the anonymous reviewers of this paper for their helpful comments and suggestions. This work was supported in part by Strategic Programs for R&D (President's Discretionary Fund) of RIKEN and Grants-in-Aid for Scientific Research of Japan (19800062, 20700175, and 20113007).

References

1. M. A. Balafar, A. R. Ramli, M. I. Saripan, and S. Mashohor. Review of brain mri image segmentation methods. *Artif. Intell. Rev.*, 33:261–274, 2010.
2. A. Bartoli. Maximizing the predictivity of smooth deformable image warps through cross-validation. *J. Math. Imaging Vis.*, 31(2-3):133–145, 2008.
3. A. Belyaev. On transfinite barycentric coordinates. In *Proc. of Eurographics Symp. on Geometry processing*, pages 89–99. Eurographics Association, 2006.
4. H. Bhaskar and S. Singh. Live cell imaging: a computational perspective. *J. of Real-Time Image Processing*, 1:195–212, 2007.

- 14 S. YOSHIZAWA, S. TAKEMOTO, M. TAKAHASHI, M. MUROI, S. KAZAMI, H. MIYOSHI, and H. YOKOTA
5. M. Botsch and L. Kobbelt. Real-time shape editing using radial basis functions. *Comput. Graph. Forum*, 24(3):611–621, 2005.
6. A. Buades, B. Coll, and J. M. Morel. A non-local algorithm for image denoising. In *Proc. of IEEE Conf. on Computer Vision and Pattern Recognition*, pages 60–65, 2005.
7. J. C. Carr, R. K. Beatson, J. B. Cherrie, T. J. Mitchell, W. R. Fright, B. C. McCallum, and T. R. Evans. Reconstruction and representation of 3d objects with radial basis functions. In *Proceedings of ACM SIGGRAPH*, pages 67–76. ACM, 2001.
8. G. Cong and B. Parvin. Model based segmentation of nuclei. In *Proc. of IEEE Conf. on Computer Vision and Pattern Recognition*, volume 1, page 256261, 1999.
9. O. Dzyubachyk, W. A. Cappelen, J. Essers, W. Niessen, and E. Meijering. Energy minimization methods for cell motion correction and intracellular analysis in live-cell fluorescence microscopy. In *Proc. of IEEE Int. Symp. on Biomedical Imaging*, pages 1127–1130. IEEE, 2009.
10. R. Eils and C. Athale. Computational imaging in cell biology. *J. Cell Biol.*, 161:477–481, 2003.
11. M. Fornefett, K. Rohr, and H. S. Stiehl. Elastic registration of medical images using radial basis functions with compact support. In *Proc. of IEEE Conf. on Computer Vision and Pattern Recognition*, pages 402–407, 1999.
12. V. Gay-Bellile, A. Bartoli, and P. Sayd. Direct estimation of nonrigid registrations with image-based self-occlusion reasoning. *IEEE Trans. on Pattern Analysis and Machine Intelligence*, 32(1):87–104, 2010.
13. G. Gilboa and S. Osher. Nonlocal linear image regularization and supervised segmentation. *Multiscale Model. Simul.*, 6:595–630, 2007.
14. R. D. Goldman and D. L. Spector. *Live Cell Imaging: A Laboratory Manual*. Cold Spring Harbor Laboratory Press, 2004.
15. R. C. Gonzalez and R. E. Woods. *Digital Image Processing*. Pearson Education Inc., 2008.
16. N. Harder, R. Eils, and K. Rohr. Automated classification of mitotic phenotypes of human cells using fluorescent proteins. *Methods in Cell Biology*, 85:539–554, 2008.
17. L. He, Z. Peng, B. Everding, X. Wang, C. Y. Han, K. L. Weiss, and W. G. Wee. Review: A comparative study of deformable contour methods on medical image segmentation. *Image Vision Comput.*, 26:141–163, 2008.
18. M. Hernandez, M. Bossa, and S. Olmos. Registration of anatomical images using paths of diffeomorphisms parameterized with stationary vector field flows. *International Journal of Computer Vision*, 85(3):291–306, 2009.
19. N. Houhou, X. Bresson, A. Szlam, T.F. Chan, and J.P. Thiran. Semi-supervised segmentation based on non-local continuous min-cut. In *Int. Conf. on Scale Space and Variational Methods in Computer Vision*, pages 112–123, 2009.
20. I.-H. Kim, S. Yang, P. Le Baccon, E. Heard, Y.-C. Chen, D. Spector, C. Kappel, R. Eils, and K. Rohr. Non-rigid temporal registration of 2d and 3d multi-channel microscopy image sequences of human cells. In *Proc. of IEEE Int. Symp. on Biomedical Imaging*, pages 1328–1331. IEEE, 2007.
21. J. I. Starck, F. Murtagh, and M. Louys. Astronomical image compression using the pyramidal median transform. In *Proc. of Astron. Data Anal. Software Syst. IV*, pages 268–271, 1995.
22. Y. Liu. Automatic range image registration in the markov chain. *IEEE Trans. on Pattern Analysis and Machine Intelligence*, 32(1):12–29, 2010.
23. J. B. A. Maintz and M. A. Viergever. A survey of medical image registration. *Medical Image Analysis*, 2(1):1–16, 1998.
24. J. Mattes, J. Nawroth, P. Boukamp, R. Eils, and K. M. Greulich-Bode. Analyzing motion and deformation of the cell nucleus for studying co-localizations of nuclear structures. In *Proc. of IEEE Int. Symp. on Biomedical Imaging*, pages 1044–1047. IEEE, 2006.
25. U. Maulik. Medical image segmentation using genetic algorithms. *Trans. Info. Tech. Biomed.*, 13:166–173, 2009.

26. D. P. McCullough, P. R. Gudla, B. S. Harris, J. A. Collins, K. J. Meaburn, M. A. Nakaya, T. P. Yamaguchi, T. Misteli, and S. J. Lockett. Segmentation of whole cells and cell nuclei from 3-D optical microscope images using dynamic programming. *IEEE Trans. on Medical Imaging*, 27(5):723–734, 2008.
27. J. McQueen. Some methods for classification and analysis of multivariate observations. In *Proc. of the Fifth Berkeley Symp. on Mathematical Statistics and Probability*, pages 281–297, 1967.
28. V. Melnik, I. Shmulevich, K. Egiazarian, and J. Astola. Image denoising using a block-median pyramid. In *Proc. of IEEE Int. Conf. on Image Processing*, volume 4, pages 162–166. IEEE, 1999.
29. J. Nakanishi, Y. Kikuchi, S. Inoue, K. Yamaguchi, T. Takarada, and M. Maeda. Spatiotemporal control of migration of single cells on a photoactivatable cell microarray. *J. Am. Chem. Soc.*, 129(21):6694–6695, 2007.
30. Y. Ohtake, A. Belyaev, and H.-P. Seidel. 3D scattered data approximation with adaptive compactly supported radial basis functions. In *Proc. of Shape Modeling International*, pages 31–39. IEEE Computer Society, 2004.
31. M. J. L. Orr. Regularisation in the selection of radial basis function centres. *Neural Computation*, 7:606–623, 1995.
32. W. H. Press, S. A. Teukolsky, W. T. Vetterling, and B. P. Flannery. *Numerical Recipes 3rd Edition: The Art of Scientific Computing*. Cambridge University Press, 2007.
33. T. Rhee, J. P. Lewis, K. Nayak, and U. Neumann. Adaptive non-rigid registration of 3D knee MRI in different pose spaces. In *Proc. of IEEE Int. Symp. on Biomedical Imaging*, pages 1111–1114. IEEE, 2008.
34. B. Rieger, C. Molenaar, R. W. Dirks, and L. J. Van Vliet. Alignment of the cell nucleus from labeled proteins only for 4D in vivo imaging. *Microsc. Res. Tech.*, 64(2):142–150, 2004.
35. O. Schmitt, J. Modersitzki, S. Heldmann, S. Wirtz, and B. Fischer. Image registration of sectioned brains. *Int. J. of Computer Vision*, 73(1):5–39, 2007.
36. A. M. Siddiqui, A. Masood, and M. Saleem. A locally constrained radial basis function for registration and warping of images. *Pattern Recognition Letter*, 30(4):377–390, 2009.
37. J. L. Starck, D. L. Donoho, and E. J. Candoès. Astronomical image representation by the curvelet transform. *Astron. Astrophys.*, 398(2):785–800, 2002.
38. J. P. Thirion. Image matching as diffusion process: an analogy with Maxwell’s demons. *Medical Image Analysis*, 2:243–260, 1998.
39. G. Turk, H. Q. Dinh, J. F. O’Brien, and G. Yngve. Implicit surfaces that interpolate. In *Proc. of Int. Conf. on Shape Modeling & Applications*, pages 62–74. IEEE Computer Society, 2001.
40. G. Wu, F. Qi, and D. Shen. A general learning framework for non-rigid image registration. In *Medical Imaging and Augmented Reality*, pages 219–227, 2006.
41. S. Yang, D. Köhler, K. Teller, T. Cremer, P. Le Baccon, E. Heard, R. Eils, and K. Rohr. Non-rigid registration of 3-D multichannel microscopy images of cell nuclei. *IEEE Trans. on Image Processing*, 17(4):493–499, 2008.
42. S. Yoshizawa, S. Takemoto, M. Takahashi, M. Muroi, S. Kazami, H. Miyoshi, and H. Yokota. Intracellular volume registration. In *Proc. of Int. Conf. on Intelligent Systems Design and Applications*, pages 1407–1412. IEEE Computer Society, 2009.
43. H. Zhang, J. E. Fritts, and S. A. Goldman. Image segmentation evaluation: A survey of unsupervised methods. *Comput. Vis. Image Underst.*, 110(2):260–280, 2008.
44. B. Zitová and J. Flusser. Image registration methods: A survey. *Image and Vision Computing*, 21(11):977–1000, 2003.
45. B. Zitová, J. Flusser, and F. Šroubek. Image registration: A survey and recent advances. In *Tutorial of IEEE Int. Conf. on Image Processing*, pages 1–2. IEEE, 2005.

16 S. YOSHIZAWA, S. TAKEMOTO, M. TAKAHASHI, M. MUROI, S. KAZAMI, H. MIYOSHI, and H. YOKOTA

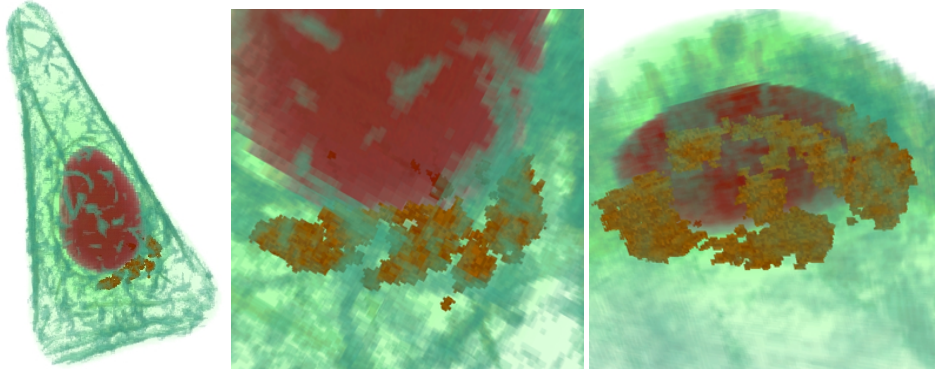


Fig. 13. Two organellar volumes (actin filaments and Golgi apparatus) are combined where the corresponding reference volumes are shown in the most left images of Figure 15.

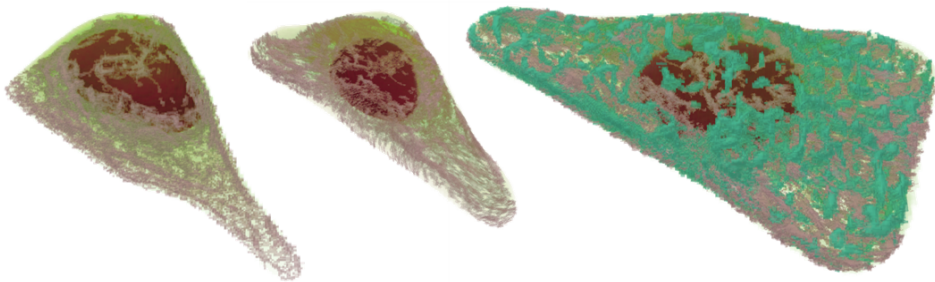


Fig. 14. Left: the target and reference volumes of microtubules. Center: the volume of microtubules mapped onto the actin's reference volume. Right: the registration result of two organellar volumes (actin filaments and microtubules).

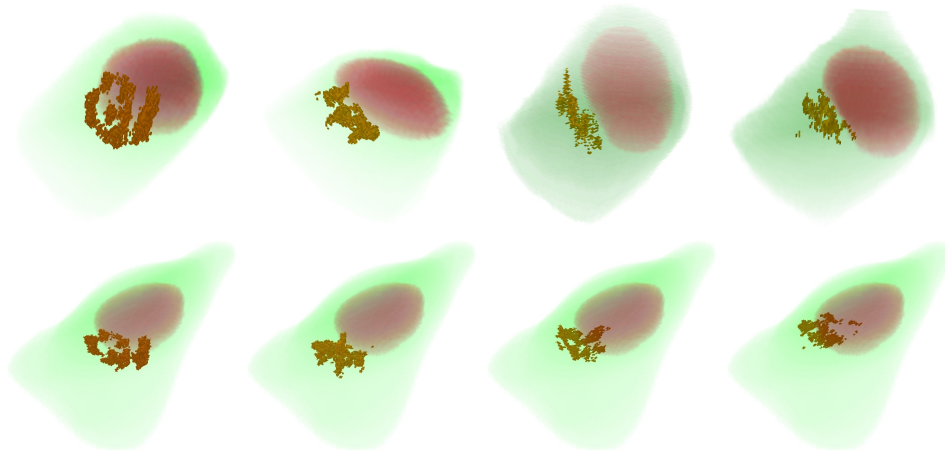


Fig. 15. Examples of registration by our approach. Four different Golgi apparatus volumes (top) are successfully mapped onto another reference volume (bottom). The top four volume data were collected from one living cell with varying time.